Check for updates

Promotion effect of urchin-like MnO$_x$@PrO$_x$ hollow core–shell structure catalysts for the low-temperature selective catalytic reduction of NO with NH$_3$

Shuyuan Cheng, [ID] [a] Jing Shao,[a] Bichun Huang,*[abc] Jinkun Guan[a] and Lusha Zhou[a]

A MnO$_x$@PrO$_x$ catalyst with a hollow urchin-like core–shell structure was prepared using a sacrificial templating method and was used for the low-temperature selective catalytic reduction of NO with NH$_3$. The structural properties of the catalyst were characterized by FE-SEM, TEM, XRD, BET, XPS, H$_2$-TPR and NH$_3$-TPD analyses, and the performance of the low-temperature NH$_3$-SCR was also tested. The results show that the catalyst with a molar ratio of Pr/Mn = 0.3 exhibited the highest NO conversion at nearly 99% at 120 °C and NO conversion greater than 90% over the temperature range of 100–240 °C. Also, the MnO$_x$@PrO$_x$ catalyst presented desirable SO$_2$ and H$_2$O resistance in 100 ppm SO$_2$ and 10 vol% H$_2$O at the space velocity of 40 000 h^{-1} and a testing time of 3 h test at 160 °C. The excellent low-temperature catalytic activity of the catalyst could ultimately be attributed to high concentrations of Mn^{4+} and adsorbed oxygen species on the catalyst surface, suitable Lewis acidic surface properties, and good reducing ability. Additionally, the enhanced SO$_2$ and H$_2$O resistance of the catalyst was primarily ascribed to its unique core–shell structure which prevented the MnO$_x$ core from being sulfated.

1 Introduction

The selective catalytic reduction of NO with NH$_3$ (NH$_3$-SCR) is considered to be the most effective and widely applied technology for eliminating NO$_x$ from stationary sources.[1–3] Low-temperature NH$_3$-SCR, which can be placed downstream of a desulfurization tower and electrostatic precipitation in a power generation system, has gained increasing attention in recent years due to improved SCR economics.[4] Abundant investigations have been carried out, and have made great progress in low-temperature NH$_3$-SCR catalysts. Many developments have been made on low-temperature NH$_3$-SCR catalysts. Among the various catalyst systems, Cu-based,[5,6] Ce-based,[7] Fe-based,[8,9] Zr-based,[10] Mn-contained catalysts have stimulated great interest because of their oxidation–reduction properties, environmentally friendly features and excellent low-temperature activities, however a disadvantage is easy deactivation in the presence of SO$_2$ in the exhaust gas.

Many strategies have been proposed to overcome this problem. One strategy includes adding other metal elements modification and is considered as one of the most promising and effective methods. Wang et al.[11] reported that the co-doping with Fe and Co can effectively improve the SO$_2$ resistance of a Mn–Ce/TiO$_2$ catalyst because the introduction of Fe and Co can prevent SO$_2$ diffusion to the inner layer of the catalyst. Chang et al.[12] proposed that the SO$_2$ resistance of MnO$_x$–CeO$_2$ could be enhanced by Sn doping since it creates more Lewis acid sites on the surface for the SO$_2$-containing SCR reaction. Xie et al.[13] demonstrated that the addition of Cr reduced the SO$_2$ adsorption strength on the surface of a MnCrO$_x$/sepiolite catalyst, thereby increasing the anti-SO$_2$ poisoning of the catalyst.

Among the potential additives, rare earth oxides (REOs) have been proven to possess high catalytic activity originating from their oxygen vacancies and strong surface acidities.[14–18] Yan et al.[18] synthesized RE-doped Mn/ASC for the low-temperature NH$_3$-SCR of NO and found that the addition of RE enhanced the catalytic activity. In addition, DRIFTS result confirm that Ce doping provides more active Brønsted acid sites. Yu et al.[19] studied the de-NO$_x$ catalytic activity and SO$_2$ resistance of Ce/Pr-MnO$_x$/SAPO-34 and proposed that compared with Ce, the Pr doping on the MnO$_x$/SAPO-34 contained more oxygen vacancies, exhibited a superior low-temperature NH$_3$-SCR activity, and inhibited the formation of ammonia sulfate on the catalyst surface, which protected the active Mn sites.

[a]School of Environment and Energy, South China University of Technology, Guangzhou Higher Education Mega Centre, Guangzhou 510006, P. R. China. E-mail: cebhuang@scut.edu.cn

[b]Guangdong Provincial Key Laboratory of Atmospheric Environment and Pollution Control, South China University of Technology, Guangzhou Higher Education Mega Centre, Guangzhou 510006, P. R. China

[c]The Key Lab of Pollution Control and Ecosystem Restoration in Industry Clusters, Ministry of Education, South China University of Technology, Guangzhou Higher Education Mega Centre, Guangzhou 510006, P. R. China

Some researchers contend that the morphology and structure of the composite oxide catalysts had an impact on their resistance to SO_2 poisoning in the low-temperature SCR process.[20–24] Generally, compared with irregular particles, catalysts with a well-designed structure typically exhibit higher functionality due to the size, shape, and interfacial effects. Therefore, considerable research has been focused on preparing SCR catalysts with a specific structure, such as hierarchical porous structures, hollow structures or a core–shell structure. In particular, core–shell structured catalysts have attracted much attention due to their unique mechanical and structural properties for the low-temperature NH_3-SCR. For instance, a $MnO_x@TiO_2$ core–shell nanorod catalyst was prepared by a novel two-step method, which exhibited outstanding SCR performance due to possessed abundant mesopores and a core–shell structure. These features protect the catalytic active sites from SO_2 and H_2O poisoning.[2] Han *et al.* designed a *meso*-$TiO_2@Fe_2O_3@Al_2O_3$ core–shell material using experimental and density functional theory methods and found that the strong SO_2 tolerance was attributed to the mesoporous-TiO_2 shell, and it effectively prevented the deposition of $FeSO_4$ and NH_4HSO_4.[25] Ma *et al.* synthesized a hollow structured CeO_2–MnO_x hybrid materials with a multi-shelled structure by using carbon spheres as the hard template. This hybrid material displayed superior activity and stability over traditional CeO_2–MnO_x particles, most likely attributed to the special multi-shelled structure and abundant surface active species.[26] Hence, the controlled fabrication of well-structured composites is of great significance for low-temperature NH_3-SCR catalysts, and the core shape, elements and shell thicknesses are key factors. The hollow, core–shell composite structure catalyst, with special isolated chambers and controllable shell structures, would be prepared according to the structural characteristics of the hollow structure and core–shell structure. To the best of our knowledge, there are a limited number of reports about the hollow, core–shell structured Mn–Pr binary oxides as catalysts for low-temperature NH_3-SCR.

In this paper, a hollow $MnO_x@PrO_x$ core–shell structure catalyst for the low-temperature NH_3-SCR reaction was prepared using carbon spheres both as hard template and as reducing agent. The obtained catalysts were then characterized by SEM, TEM, XRD, XPS, NH_3-TPD and H_2-TPR analysis, and the NH_3-SCR reaction performance was tested to determine the physicochemical properties and structure–performance relationships.

2 Experimental

2.1 Catalyst preparation

Carbon spheres were prepared according to a typical hydrothermal method.[27] Typically, a 60 mL solution containing 0.5 g glucose was hydrothermally treated at 180 °C for 24 h and then cooled to room temperature naturally. After suction, filtering and washing with deionized water and absolute ethanol, the dark brown sample was dried in a vacuum oven at 80 °C for 12 h, and the templates were obtained.

The chemical process to synthesize the hollow $MnO_x@PrO_x$ was carried out in two steps. The $CSs@MnO_x$ was first synthesized with the following procedure. A desired amount of CSs was placed into deionized water, and then $KMnO_4$ was added with unceasingly stirring for 30 min. Thereafter, the mixture solution was transferred into an autoclave and maintained at 160 °C for 12 h. Until cooling to room temperature naturally, the obtained suspension was centrifuged and washed with water and absolute ethanol repeatedly. Finally, the $CSs@MnO_x$ was obtained by drying at 80 °C for 12 h.

Second, the hollow $MnO_x@PrO_x$ was synthesized by a chemical precipitation method. Certain amounts of $CSs@MnO_x$, $Pr(NO_3)_3·6H_2O$, and NaOH were respectively dissolved in deionized water with the molar ratios of Pr/Mn of 0.3 and $Pr(NO_3)_3·6H_2O/NaOH$ of 0.5. Thereafter, the $Pr(NO_3)_3·6H_2O$ and NaOH solutions were added dropwise into above solution simultaneously and heated to 85 °C under stirring for 3 h. Finally, the hollow $MnO_x@PrO_x$ was collected, washed to neutral, dried at 80 °C for 12 h and calcined at 400 °C in air for 3 h. The hollow MnO_x could be obtained by the roasting treatment of $CSs@MnO_x$. The hollow MnO_x–PrO_x catalyst without a core–shell structure was prepared through a similar method for hollow MnO_x, and the only difference was that $KMnO_4$ and $Pr(NO_3)_3·6H_2O$ were added together.

2.2 NH_3-SCR activity test

The NH_3-SCR activity of the solid catalyst was carried out in a fixed-bed quartz continuous flow reactor. The feed gas was composed of 0.08% NO, 0.08% NH_3, 100 ppm SO_2 (when added), 10 vol% H_2O (when added), 5.0 vol% O_2, and the balanced gas was Ar. The total flow rate was 600 mL min^{-1}, corresponding to a gas hourly space velocity (GHSV) of 40 000 h^{-1}. The NO, NO_2 and NO_x concentrations were measured using an NO–NO_2–NO_x analyzer (Thermal Scientific, model 42i-HL), and the concentration of N_2 was monitored using a gas chromatograph (GC9560, Shanghai Huaai) with a TCD and 5 A columns. The NO removal efficiency and the N_2 selectivity were obtained by the following equations:

$$NO\ conversion(\%) = \frac{C_{NO}^{in} - C_{NO}^{out}}{C_{NO}^{in}} \times 100 \qquad (1)$$

$$N_2\ selectivity(\%) = \frac{C_{NO}^{in} + C_{NH_3}^{in} - C_{NO}^{out} - C_{NH_3}^{out} - C_{NO_2}^{out} - 2C_{N_2O}^{out}}{C_{NO}^{in} + C_{NH_3}^{in} - C_{NO}^{out} - C_{NH_3}^{out}}$$
$$\times 100 \qquad (2)$$

2.3 Catalyst characterization

Field emission scanning electron microscopy (FE-SEM) with an energy dispersive spectroscopy (EDS) was used to analyze the surface morphology and elemental composition of the catalysts using a ZEISS Merlin instrument. The micro-structural characterization by transmission electron microscopy (TEM) and high-resolution TEM (HRTEM) were carried out on JEM-2100 HT. Elemental mapping was conducted using an Inca Energy 200 TEM system. X-ray diffraction (XRD) was determined using a D8
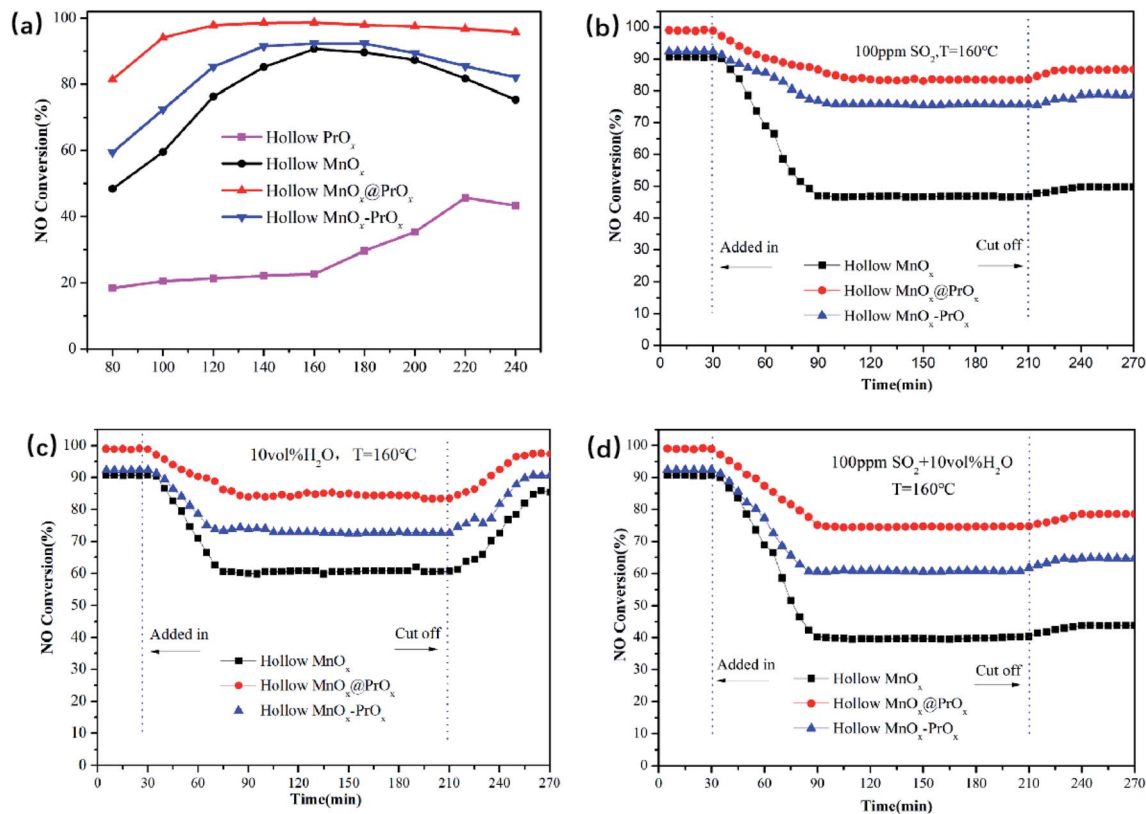
Fig. 1 NO conversion (a); SO$_2$ (b); H$_2$O (c); SO$_2$ + H$_2$O (d) tolerance test of catalysts.

Advance (Bruker) X-ray diffraction instrument with Cu Kα radiation (λ = 1.5406 Å). X-ray photo-electron spectroscopy (XPS) analyses were carried out on an ESCALAB 250 spectrometer (Thermo Fisher Scientific, USA) equipped with Al Kα X-ray radiation (1486.7 eV). H$_2$-TPR (10% H$_2$/Ar gas flow: 30 mL min^{-1} and a heating rate of 10 °C min^{-1}) and NH$_3$-TPD (N$_2$ flow: 30 mL min^{-1} and a heating rate of 10 °C min^{-1}) analysis were performed using a Micromeritics Auto ChemII 2920 instrument.

3 Results and discussion

3.1 Catalytic performance for the low-temperature NH$_3$-SCR

The NH$_3$-SCR catalytic performance of the hollow PrO$_x$, hollow MnO$_x$, hollow MnO$_x$@PrO$_x$ and hollow MnO$_x$–PrO$_x$ were shown in Fig. 1a. It could be seen from Fig. 1a that the NO conversion of the MnO$_x$-containing samples increased with increasing reaction temperature and then decreased, exhibiting different activated temperature windows. Comparatively, the hollow PrO$_x$
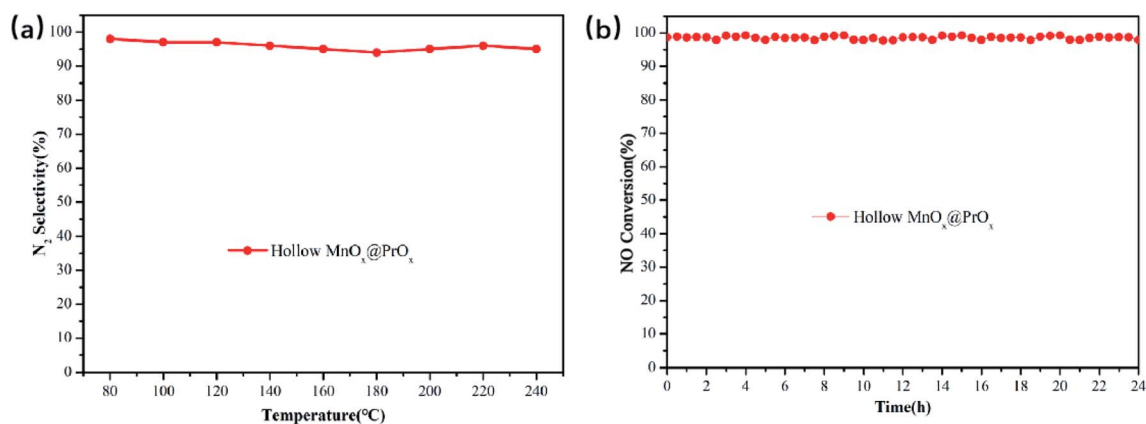

Fig. 2 N$_2$ selectivity (a) and stability test (b) of hollow MnO$_x$@PrO$_x$.

catalyst basically had no catalytic activity at low temperature, when the reaction temperature greater than 160 °C, and the NO conversion rate began to gradually increase and reached the maximum conversion rate about 45% at 220 °C. Comparing the four catalysts, the hollow $MnO_x@PrO_x$ catalyst exhibited superior low-temperature catalytic activity, achieving 97.1% of NO conversion at 100 °C, while the hollow PrO_x, hollow MnO_x and hollow $MnO_x–PrO_x$ were only 21.3%, 59.5%, and 72.4%, respectively. In addition, the hollow $MnO_x@PrO_x$ catalyst displayed more than 90% NO conversion over a wider temperature range of 100–240 °C, while the other catalysts had narrow temperature windows. N_2 selectivity tests (Fig. 2a) and stability tests (Fig. 2b) were also performed and the hollow $MnO_x@PrO_x$ consistently exhibited excellent catalytic activity, high N_2 selectivity and high stability. In the whole reaction temperature range of 80–240 °C, N_2 selectivity was above 95%, and NO conversion was maintained at 97% over the 24 h stability test at 160 °C. It could be deduced that the core–shell structure promotes the synergistic effect between the MnO_x core and PrO_x shell, and enhanced catalytic activity.

The effects of SO_2 and H_2O on the low-temperature SCR activity of catalysts are shown in Fig. 1(b–d). Fig. 1b shows the NO conversion for the hollow MnO_x, hollow $MnO_x@PrO_x$ and hollow $MnO_x–PrO_x$ catalysts when 100 ppm SO_2 was added at 160 °C. NO conversion decreased upon the addition of SO_2. The hollow $MnO_x@PrO_x$ exhibited superior resistance to SO_2 poisoning, and the NO conversion was maintained at over 83.4% after a 3 h test, while the NO conversion of hollow $MnO_x–PrO_x$ decreased from 92.3% to 75.5%. And the hollow MnO_x catalyst exhibited a more obvious poisoning and the NO conversion decreased from 90.7% to 46.3%. Furthermore, when SO_2 steam was cut off, the NO conversion for the catalysts could be partly restored to 86.6%, 78.7% and 49.7%, respectively. As displayed in Fig. 1c, the H_2O

resistance of the catalysts was tested using 10 vol% H_2O at 160 °C. A decrease in NO conversion from 90.6% to less than 60% for the hollow MnO_x catalyst was detected. In addition, the NO conversions of hollow $MnO_x@PrO_x$ and hollow $MnO_x–PrO_x$ declined as well but still remained at around 84% and 73%, respectively, for the next three hours. Additionally, it is worth noting that the NO conversion with the catalysts almost recovered to its original level when H_2O was completely removed, indicating that the inhibitory effect of H_2O are reversible. According to the results shown in Fig. 1d, when 100 ppm SO_2 and 10 vol% H_2O were both introduced into the reaction system, the NO conversions of the catalysts were lower than in the presence of either SO_2 or H_2O alone. This was especially seen using the hollow MnO_x catalyst, which exhibited relatively faster deactivation with NO conversion decreasing sharply from 90.5% to 39.4% within one hour. By comparison, the coexistence of SO_2 and H_2O only resulted in a 20% decrease in NO conversion for the hollow $MnO_x@PrO_x$ and a 32% decrease for hollow $MnO_x–PrO_x$, indicating that the introduction of Pr element could not only significantly increase the low-temperature activity of the catalysts but also enhance the SO_2 and H_2O resistance of the catalysts. The excellent poisoning resistance of the hollow $MnO_x@PrO_x$ catalyst could be attributed to the protective effect of the PrO_x shell, which could first react with SO_2 and restrain the formation of manganese sulfate. Compared with other catalytic systems,[28–30] the poisoning resistance of the hollow $MnO_x@PrO_x$ catalyst was relatively better than the other tested catalysts.

3.2 Structural characterization of catalysts

3.2.1 FE-SEM and TEM analysis. The morphology of the synthesized catalysts was characterized by FE-SEM (Fig. 3). Fig. 3a shows the uniform and smooth carbon spheres (CS_s),
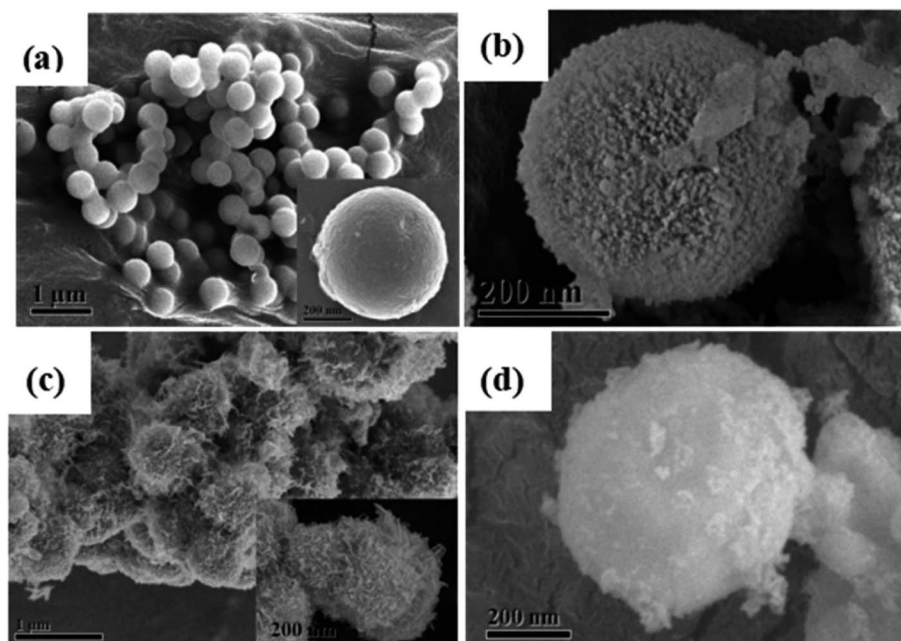

Fig. 3 Low and high-magnification FE-SEM images of CSs (a); hollow MnO_x (b); hollow $MnO_x@PrO_x$ (c) and hollow $MnO_x–PrO_x$ (d).

which served as both the sacrificial templates and as reducing agents. After the oxidation–reduction reaction between the $KMnO_4$ solution and CS_s, MnO_x particles were grown *in situ* on the CSs surface (Fig. 3b), and maintained their spherical structure. As shown in Fig. 3c, the hollow $MnO_x@PrO_x$ catalyst was comprised of uniform spheres that were fully coated by the 1D nanosheets, and exhibited an urchin-like structure. The morphology of the hollow MnO_x–PrO_x was wrinkled when accompanied with combustion of CSs during calcination but almost retained its original morphology (Fig. 3d).

The structural information of the catalysts were further investigated by TEM and HRTEM (Fig. 4). Fig. 4a and d revealed that the hollow $MnO_x@PrO_x$ catalyst exhibited an apparent interface between the hollow core and shell, indicating the typical features of a hollow core–shell architecture. The hollow core was about 40 nm in thickness with a 400 nm cavity and the nanosheet shell layer was about 60 nm in thickness. In addition, the TEM images of the hollow MnO_x (Fig. 4c and f) and hollow MnO_x–PrO_x (Fig. 4g and h) displayed visibly hollow structures with shell layers of about 40 nm and 100 nm in

thickness, respectively. The TEM images were in agreement with the FE-SEM images, and the *d*-spacing value was determined from the HR-TEM images and identified in the corresponding crystals. As shown in Fig. 4b and e, the highly crystalline lattice fringes with an inter-fringe spacing of 0.69 nm and 0.27 nm corresponded to the (110) plane of α-MnO_2 (ref. 31) and the (222) plane of Mn_2O_3.[32] Lattice fringes with a spacing of 0.28 nm, 0.38 nm and 0.31 nm were indexed to the Pr_2O_3 (402), (202) planes[33,34] and the PrO_2 (111) plane,[35] respectively, indicating that the hollow MnO_x nanospheres were coated by a shell of PrO_x nanosheets. However, a hollow mixed oxide was observed in the hollow MnO_x–PrO_x (Fig. 4i). Ma *et al.*[26] suggested that the homogeneous elemental distribution was favorable to the synergistic effects between elements, indicating that there existed intimate interactions between MnO_x and PrO_x.

The composition and distribution of the corresponding elements in the hollow $MnO_x@PrO_x$ were evaluated by EDS and elemental mapping. EDS analysis in Fig. 5a shows that the hollow $MnO_x@PrO_x$ was composed of Mn, Pr and O. In
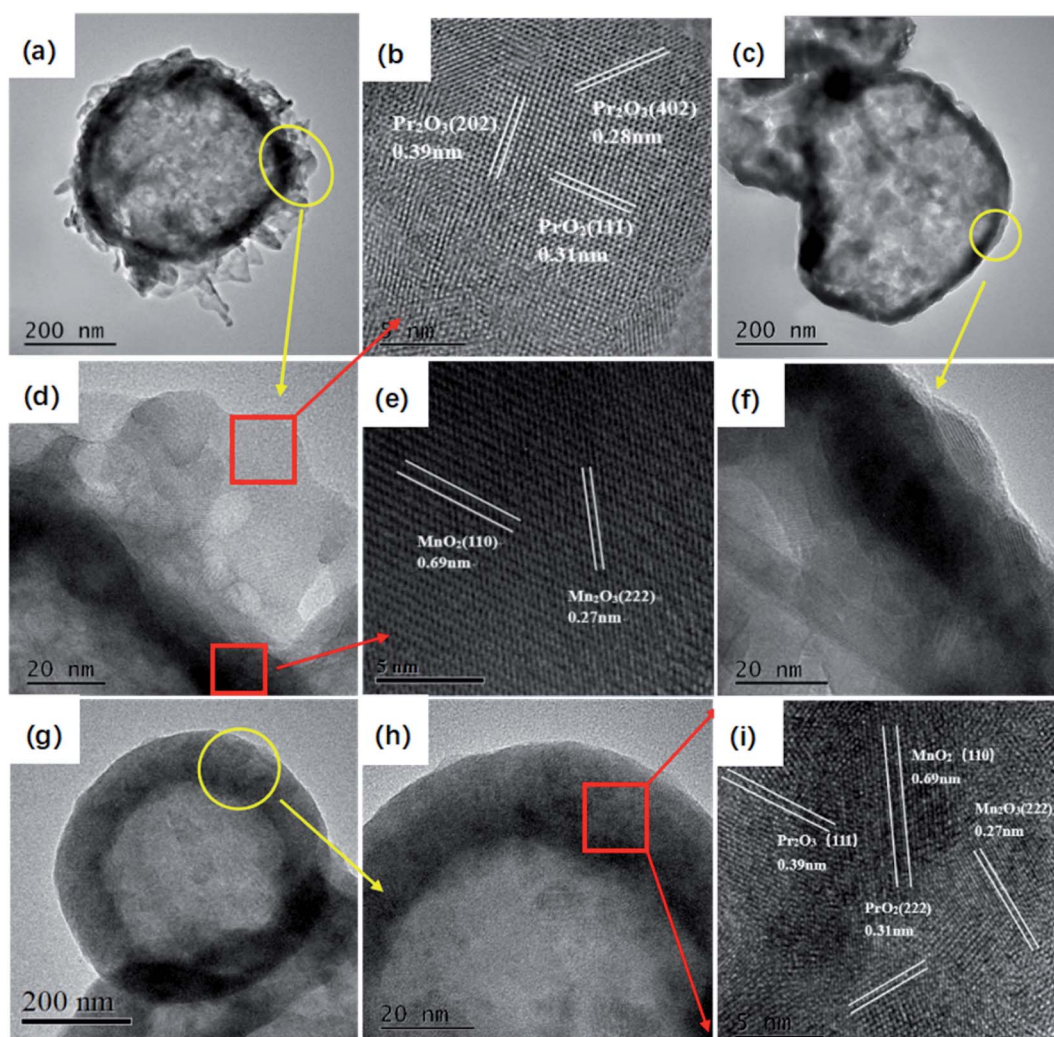

Fig. 4 TEM and FE-TEM images with different magnifications of hollow $MnO_x@PrO_x$ (a, b, d and e) and hollow MnO_x (c and f) and hollow MnO_x–PrO_x (g–i).
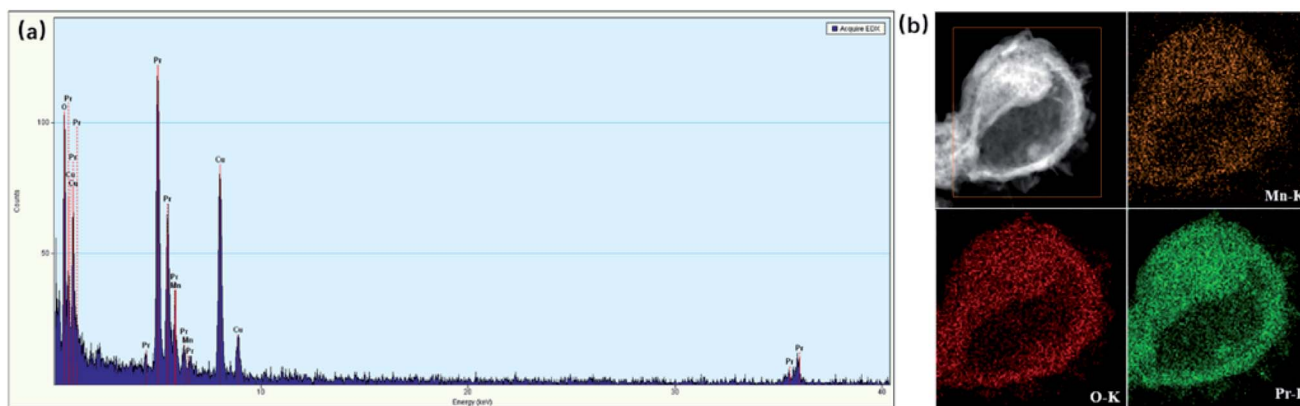
Fig. 5 EDS spectra (a) and HAADF-STEM images (b) of an individual hollow $MnO_x@PrO_x$, and its element mapping of O, Mn and Pr.

addition, the elemental map in Fig. 5b further revealed that each type of atom was uniformly distributed within the entire structure. The Pr species were located in the external layer of the hollow urchin-shaped structure, and the Mn species were observed in the interior layer. Also, the distribution range of the Pr was found to be the same as Mn, demonstrating that the PrO_x uniformly covered the MnO_x core. Based on the results above, it is reasonable to deduce that the core–shell structure catalyst could not only provide a relatively enclosed micro-environment to expose abundant active sites and enhance mass transfer, but the PrO_x shell also protected the MnO_x core from being poisoned. This contributed to an excellent SO_2/H_2O-tolerance of the hollow $MnO_x@PrO_x$ catalyst.

3.2.2 XRD and BET analysis. XRD tests were carried out to determine the component and crystal phase structures of the catalysts. The crystalline structure of the active component plays an important role in its catalytic performance. Fig. 6 exhibits the typical XRD pattern of the catalysts including CSs, hollow MnO_x and hollow $MnO_x@PrO_x$. For the CSs templates, only a distinct diffraction peak at 24° was detected, which was associated with the carbon material.[36] Interestingly, no characteristic peaks of CSs were observed in the hollow MnO_x, hollow $MnO_x@PrO_x$, or hollow $MnO_x–PrO_x$, suggesting that the sacrificial template of CSs was completely eliminated by heating at 400 °C. With regard to the hollow MnO_x, the peaks at $2\theta = 12.8°$, 18.1°, 28.8°, 37.5°, 41.9°, 49.8°, 56.4°, 60.3°, and 69.7° were attributed to MnO_2,[37] while the peaks at $2\theta = 32.9°$, 55.2°, and 65.8° were assigned to Mn_2O_3.[38] This phenomenon demonstrated the coexistence of different Mn species in the catalyst and that MnO_2 was the main phase. After adding the Pr species, characteristic peaks at $2\theta = 28.6°$, 47.6° and 22.8°, 31.1°, 45.6° were observed for the hollow $MnO_x@PrO_x$ and hollow $MnO_x–PrO_x$, which were related to the (110), (220) planes of PrO_2 and the (202), (402), (503) planes of Pr_2O_3, respectively. The XRD results were also in agreement with the HRTEM images. Also, the diffraction peaks of both catalysts shifted slightly to higher angles, which was attributed to that the manganese ions ($Mn^{4+} = 53$ Å, $Mn^{3+} = 64.5$ Å, $Mn^{2+} = 83$ Å) being partly diffused into the PrO_x ($Pr^{4+} = 85$ Å, $Pr^{3+} = 99$ Å) lattice during the heating process, which led to lattice shrinkage.[29,30,39–41] Additionally, as compared with the hollow MnO_x, the

characteristic XRD peaks of the MnO_2 and Mn_2O_3 were weaker and wider, which revealed that smaller mixed oxide particles with a lower degree of crystallization were formed. According to some reports,[40,42,43] the decrease in crystallization degree led to increase of surface adsorbed oxygen, thus contributing to an improved SCR performance. The BET-specific surface areas of the catalysts were measured and are summarized in Table 1. It was reported that with a larger specific surface area and pore volume of the catalyst, the exposure of active sites increased and more reactants were absorbed on the surfaces.[39] As can be seen from Table 1, after introducing Pr, the surface area and pore volume increased as follows: hollow $MnO_x@PrO_x$ (195.31 m^3 g^{-1}, 0.36 cm^3 g^{-1}) > hollow $MnO_x–PrO_x$ (185.39 m^3 g^{-1}, 0.31 cm^3 g^{-1}) > hollow MnO_x (136.70 m^3 g^{-1}, 0.24 cm^3 g^{-1}). This indicated that more reactants were adsorbed on the core–shell structure hollow $MnO_x@PrO_x$ catalyst leading to an increase in the SCR reactions.

3.2.3 XPS analysis. The surface properties of the catalysts also play an important role in the NH_3-SCR reaction. Hence, the surface atom concentrations and states of the catalysts were determined by XPS (Fig. 7 and Table 1). The XPS spectrum of
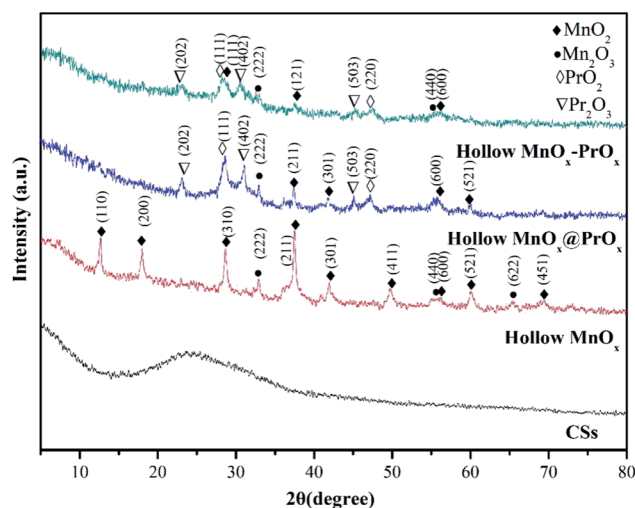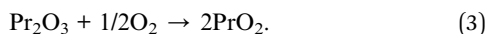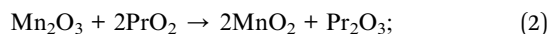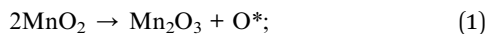

Fig. 6 XRD patterns of CSs, hollow MnO_x, hollow $MnO_x@PrO_x$ and hollow $MnO_x–PrO_x$.

Paper

Mn $2p_{3/2}$ is shown in Fig. 7a and could be divided into three peaks: Mn^{2+} (640.2–640.8 eV), Mn^{3+} (641.2–641.5 eV) and Mn^{4+} (642.5–643.0 eV).[44,45] The spectra of the hollow $MnO_x@PrO_x$ and the hollow MnO_x–PrO_x were slightly shifted to lower binding energies. Similar results have been obtained by Ma et al.[26] and Chang et al.,[46] demonstrating that the chemical environment of Mn was different from the hollow MnO_x, suggesting that there was an interaction between the MnO_x species and the PrO_x species given in the following reactions:

$$2MnO_2 \rightarrow Mn_2O_3 + O^*; \quad (1)$$

$$Mn_2O_3 + 2PrO_2 \rightarrow 2MnO_2 + Pr_2O_3; \quad (2)$$

$$Pr_2O_3 + 1/2O_2 \rightarrow 2PrO_2. \quad (3)$$

As listed in Table 1, among the three catalysts, the hollow $MnO_x@PrO_x$ possessed the highest surface molar concentration of Mn^{4+} (58.3%), indicating that the PrO_x shell might have enriched the surface concentration of the Mn^{4+} species. It was confirmed that the Mn^{4+} species and their oxidation–reduction processes were in favor of the low-temperature NH_3-SCR reaction.[44,47–49] As a result, with more Mn^{4+} species, the low-temperature catalytic activity of the catalyst was enhanced. Furthermore, it was worth noting that the concentrations of Mn significantly decreased after the coating with a PrO_x shell, which suggested that most of the Mn species were covered by PrO_x. In other words, PrO_x mainly deposited on the surface of catalyst, and the results were consistent with TEM.

The XPS spectrum of the Pr 3d reported in Fig. 7b shows two sets of spin–orbit multiples that were observed at binding energies of ca. 953.5 and 933.9 eV, which represented the $3d_{3/2}$ and $3d_{5/2}$ electrons of Pr, respectively.[50] According to He et al.,[51] the signals at ca. 928.6, 933.2, 946.3, and 951.1 eV were assigned to Pr^{3+}, and the signals at ca. 930.5, 933.9, 949.2, 953.7, and 956.8 eV to Pr^{4+}. The characteristic features of Pr^{4+} at 966–968 eV could not be resolved in the figure. As reported in other studies,[52,53] this unique peak of Pr^{4+} usually appears after oxidation treatment (O_2) of PrO_x within the XPS reactor chamber. The Pr^{4+} ions were unstable and lose electrons easily, which facilitated the process of oxygen storage and release between Pr^{4+} and Pr^{3+} ($2PrO_2 \rightarrow Pr_2O_3 + O^*$; $Pr_2O_3 + 1/2O_2 \rightarrow 2PrO_2$).[51,54] That is, the existence of Pr^{3+} in the PrO_x implied the formation of an oxygen vacancy and the ratios of $Pr^{3+}/(Pr^{3+} + Pr^{4+})$ (39.6%) in the hollow $MnO_x@PrO_x$ were higher than in the
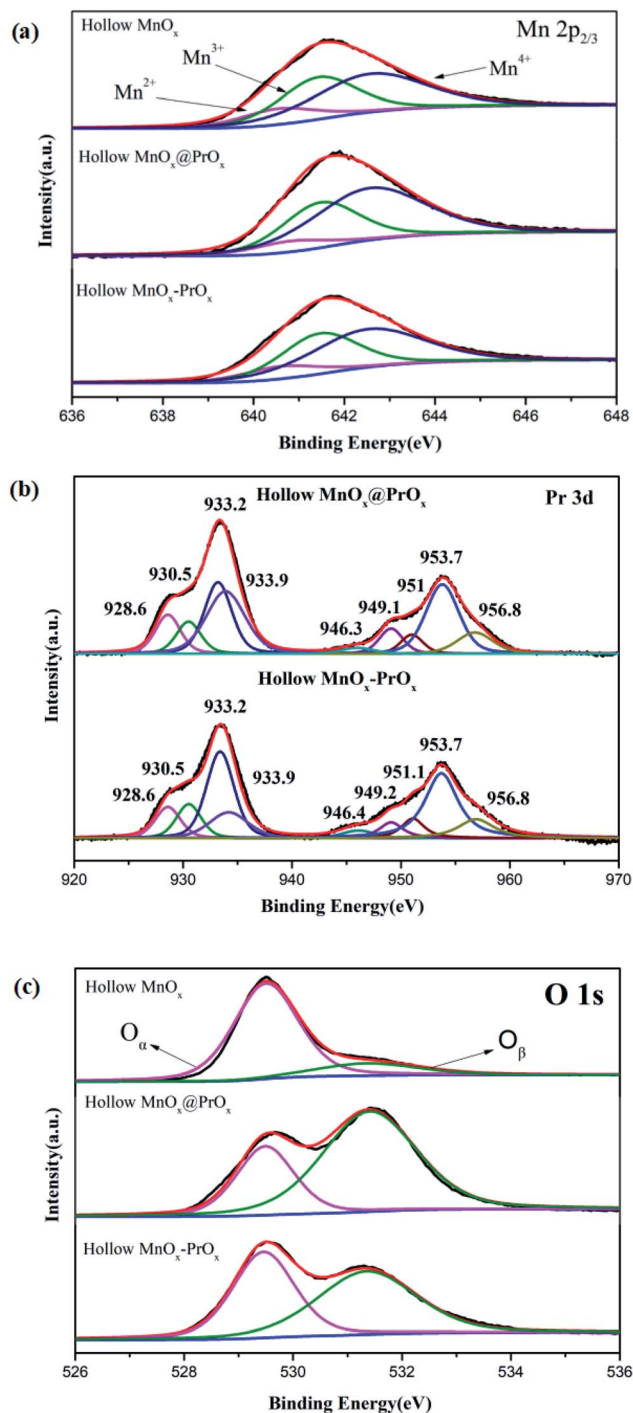
Fig. 7 XPS spectra of Mn $2p_{2/3}$ (a), Pr 3d (b) and O 1s (c) of the catalysts.

Table 1 BET surface area and surface atomic composition of the catalysts

Sample	Surface atomic concentration (%)			X_{Mn}/%			X_O/%		X_{Pr}/%		BET (m^2 g^{-1})	Pore volume (cm^3 g^{-1})
	Mn	O	Pr	Mn^{4+}	Mn^{3+}	Mn^{2+}	O_α	O_β	Pr^{4+}	Pr^{3+}		
Hollow MnO_x	39.47	60.53	—	49.01	37.02	13.97	83.05	16.95	—	—	136.70	0.24
Hollow $MnO_x@PrO_x$	12.62	54.19	33.19	58.27	33.24	8.49	29.7	70.3	60.4	39.6	195.31	0.36
Hollow MnO_x–PrO_x	34.58	50.19	15.23	51.1	37.3	11.6	57.36	42.64	66.4	33.6	185.39	0.31

Fig. 8 NH$_3$-TPD profiles of the catalysts.
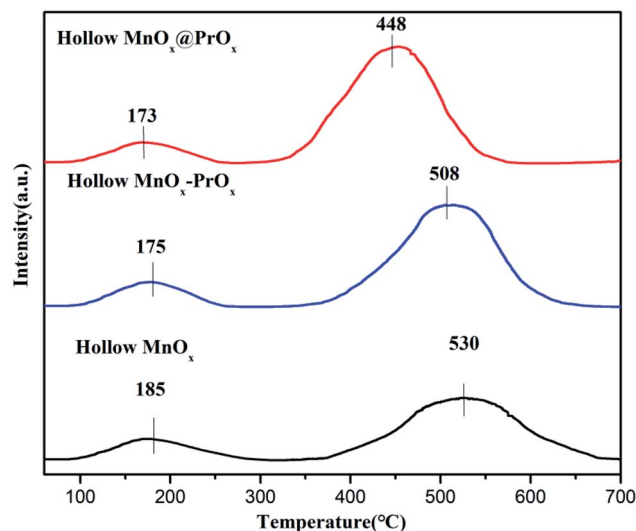

Fig. 9 H$_2$-TPR profiles of the catalysts.

hollow MnO$_x$–PrO$_x$ (33.6%). Therefore, it could be inferred that more oxygen vacancies were present in the hollow MnO$_x$@PrO$_x$ than in the hollow MnO$_x$–PrO$_x$.

The O 1s XPS spectrum for the catalysts were also shown in Fig. 7c. The sub-band at 531.3–532.2 eV was attributed to the surface-adsorbed oxygen species (O$_\beta$), and the sub-band at 529.2–530.0 eV was attributed to the lattice oxygen species (O$_\alpha$).[41] It is well known that O$_\beta$ is more active than O$_\alpha$, therefore the higher mobility of the O$_\beta$ led to better performance in the oxidation reaction. An increase in the O$_\beta$ content promoted the oxidation of NO to NO$_2$ and further enhanced the low-temperature NH$_3$-SCR reaction through a fast pathway (4NH$_3$ + 2NO + 2NO$_2$ → 4N$_2$ + 6H$_2$O).[55,56] From Table 1, the ratio of O$_\beta$/(O$_\alpha$ + O$_\beta$) in the hollow MnO$_x$@PrO$_x$ (70.3%) was the highest of the three catalysts, which agrees with the XRD analysis, and could also explain the excellent low-temperature SCR activity of the hollow MnO$_x$@PrO$_x$ catalyst.

3.2.4 NH$_3$-TPD analysis. NH$_3$-TPD was carried out to evaluate the amount of the acid sites and the acid strength of the prepared catalysts (Fig. 8 and Table 2). The TPD profile of the catalysts presented two broad desorption peaks in the temperature ranges of 100–300 °C and 400–700 °C. It was generally believed that the desorption peaks before 400 °C were ascribed to the weak adsorption of the NH$_3$ at the Brønsted acid sites, while the desorption peaks above 400 °C were ascribed to the strong adsorption of the NH$_3$ at the Lewis acid sites.[57] Moreover,
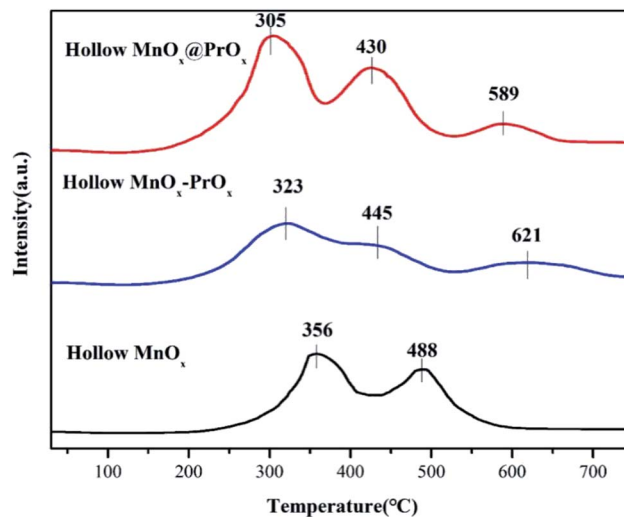
the positions of the desorption peaks were related to the acid strength and the areas of desorption peaks were related to the amount of acid sites.[3] As shown in Fig. 8, all catalysts exhibited less Brønsted acid sites but much more Lewis acid sites. In addition, in the higher temperature range, the hollow MnO$_x$@PrO$_x$ catalyst possessed the largest desorption area and the lowest desorption temperature at the Lewis acid sites, indicating that there was a sufficient number of Lewis acid sites with suitable acid strength on its surface. Studies show that the appropriate acid strength and number of sites are conducive to the adsorption-activation of NH$_3$ on the catalyst surface.[58] Moreover, the total number of acid sites for the catalysts were roughly calculated from the NH$_3$-TPD, which was listed in Table 2. The acid strength sequence of the catalysts was: hollow MnO$_x$@PrO$_x$ > hollow MnO$_x$–PrO$_x$ > hollow MnO$_x$. Based on the results, it was concluded that the hollow MnO$_x$@PrO$_x$ catalyst contained a highly effective specific surface area due to its architecture, more acid sites could be exposed, and the catalyst exhibited enhanced adsorption ability of NH$_3$, giving the same results as the BET analysis.

3.2.5 H$_2$-TPR analysis. The H$_2$-TPR test was performed to better understand the redox properties of the catalysts and the results were shown in Fig. 9. It was seen that the hollow MnO$_x$ exhibited two reduction peaks located at 356 and 488 °C, corresponding to the consecutive reduction processes of MnO$_2$–Mn$_2$O$_3$ or Mn$_3$O$_4$–MnO.[59–63] Three reduction peaks were

Table 2 The surface acidic properties of the catalysts

Sample	Peak temperature (°C)		Acid amount (mmol g^{-1})		Total acid amount (mmol g^{-1})
	T_I	T_{II}	S_I	S_{II}	
Hollow MnO$_x$@PrO$_x$	173	448	0.141	1.345	1.486
Hollow MnO$_x$–PrO$_x$	175	508	0.13	1.047	1.177
Hollow MnO$_x$	185	530	0.123	0.726	0.849

Table 3 The reducibility of the catalysts

Sample	Peak temperature (°C)			H$_2$ consumption (mmol g^{-1})			Total H$_2$ consumption (mmol g^{-1})
	T_{I}	T_{II}	T_{III}	S_{I}	S_{II}	S_{III}	
Hollow MnO$_x$@PrO$_x$	305	430	589	0.875	0.375	0.0838	1.3338
Hollow MnO$_x$–PrO$_x$	323	445	621	0.6788	0.211	0.086	0.9758
Hollow MnO$_x$	356	488	—	0.629	0.202	—	0.831

observed for the hollow MnO$_x$@PrO$_x$ and hollow MnO$_x$–PrO$_x$ with the two peaks at higher temperatures coming from the conversion of Pr^{4+} to Pr^{3+}, or the reduction reaction between Mn^{4+}/Mn^{3+} and Pr^{4+}/Pr^{3+}.[64] Specifically, the first two peaks were notably shifted to lower temperatures for both catalysts, indicating that the reduction capacity of the catalysts were improved and easier to reduce at low temperatures. In addition, the total consumption of H$_2$ for the hollow MnO$_x$@PrO$_x$ remarkably increased over the hollow MnO$_x$, as illustrated in Table 3. This implied that the addition of PrO$_x$ generated more reducing agents on the catalyst surface, which is consistent with the XPS results showing a higher reducing ability. The increased reducibility of the hollow MnO$_x$@PrO$_x$ over the hollow MnO$_x$–PrO$_x$ catalysts further proved that the special core–shell structure of the catalyst was the main reason for the excellent reducibility.

4 Conclusion

In summary, we have successfully fabricated a hollow MnO$_x$@PrO$_x$ core–shell nanohybrid as a high-performance low-temperature NH$_3$-SCR de-NO$_x$ catalyst by using a facile two-step method. The hollow MnO$_x$@PrO$_x$ nanohybrid displayed excellent low-temperature NH$_3$-SCR activity with a maximum NO conversion of 99% at 120 °C with a space velocity of 40 000 h^{-1}. It also maintained a NO conversion above 90% within the broad temperature window of 100–240 °C. This favorable catalytic behavior was mainly due to the abundant content of Mn^{4+} and O$_\beta$ species, uniform distribution of Mn and Pr species, and intimate interaction between MnO$_x$ and PrO$_x$ which brought about plentiful Lewis acid sites and excellent reducibility. Besides the excellent catalytic activity, the hollow MnO$_x$@PrO$_x$ catalyst consistently exhibited superior SO$_2$ and H$_2$O tolerance, which could be attributed to the special core–shell structure of the catalyst. The protection from the PrO$_x$ shell minimized the exposure of the hollow MnO$_x$ core surface active sites to SO$_2$ or H$_2$O, resulting in high stability and an improved anti-poisoning performance.

Conflicts of interest

There are no conflicts to declare.

Acknowledgements

References

1 T. Ryu, N. H. Ahn, S. Seo, J. Cho, H. Kim, D. Jo, G. T. Park, P. S. Kim, C. H. Kim, E. L. Bruce, P. A. Wright, I. S. Nam and S. B. Hong, Fully Copper-Exchanged High-Silica LTA Zeolites as Unrivaled Hydrothermally Stable NH$_3$-SCR Catalysts, *Angew. Chem., Int. Ed. Engl.*, 2017, **56**, 3256–3260.

2 Z. Sheng, D. Ma, D. Yu, X. Xiao, B. Huang, L. Yang and S. Wang, Synthesis of novel MnO$_x$@TiO$_2$ core-shell nanorod catalyst for low-temperature NH$_3$-selective catalytic reduction of NO$_x$ with enhanced SO$_2$ tolerance, *Chin. J. Catal.*, 2018, **39**, 821–830.

3 B. Thirupathi and P. G. Smirniotis, Nickel-doped Mn/TiO$_2$ as an efficient catalyst for the low-temperature SCR of NO with NH$_3$: catalytic evaluation and characterizations, *J. Catal.*, 2012, **288**, 74–83.

4 S. Li, B. Huang and C. Yu, A CeO$_2$-MnO$_x$ core-shell catalyst for low-temperature NH$_3$-SCR of NO, *Catal. Commun.*, 2017, **98**, 47–51.

5 Y. Cao, D. Fan, L. Sun, M. Yang, L. Cao, T. Sun, S. Xu, P. Tian and Z. Liu, The self-protection effect of reactant gas on the moisture stability of CuSAPO-34 catalyst for NH$_3$-SCR, *Chem. Eng. J.*, 2019, **374**, 832–839.

6 H. I. Hamoud, V. Valtchev and M. Daturi, Selective catalytic reduction of NO$_x$ over Cu- and Fe-exchanged zeolites and their mechanical mixture, *Appl. Catal., B*, 2019, **250**, 419–428.

7 D. Wang, Y. Peng, Q. Yang, F. Hu, J. Li and J. Crittenden, NH$_3$-SCR performance of WO$_3$ blanketed CeO$_2$ with different morphology: balance of surface reducibility and acidity, *Catal. Today*, 2019, **332**, 42–48.

8 L. Peng, Z. Li, J. Cui, C. Geng, Y. Kang, C. Zhang and C. Yang, N-doped graphene/CoFe$_2$O$_4$ catalysts for the selective catalytic reduction of NO$_x$ by NH$_3$, *RSC Adv.*, 2019, **9**, 15791.

9 N. Zhu, Z. Lian, Y. Zhang, W. Shan and H. He, Improvement of low-temperature catalytic activity over hierarchical Fe-beta catalysts for selective catalytic reduction of NO with NH$_3$, *Chin. Chem. Lett.*, 2019, **30**, 867–870.

10 S. Liu, H. Wang, Y. Wei, R. Zhang and S. Royer, Morphology-Oriented ZrO$_2$-Supported Vanadium Oxide for the NH$_3$-SCR Process: Importance of Structural and Textural Properties, *ACS Appl. Mater. Interfaces*, 2019, **11**, 22240–22254.

11 F. Wang, B. Shen, S. Zhu and Z. Wang, Promotion of Fe and Co doped Mn-Ce/TiO$_2$ catalysts for low temperature NH$_3$-SCR with SO$_2$ tolerance, *Fuel*, 2019, **249**, 54–60.

12 H. Chang, J. Li, X. Chen, L. Ma, S. Yang, J. W. Schwank and J. Hao, Effect of Sn on MnO$_x$–CeO$_2$ catalyst for SCR of NO$_x$ by

ammonia: enhancement of activity and remarkable resistance to SO₂, *Catal. Commun.*, 2012, **27**, 54–57.

13 A. Xie, Y. Tang, X. Huang, X. Jin, P. Gu, S. Luo, C. Yao and X. Li, Three-dimensional nanoflower MnCrO/sepiolite catalyst with increased SO₂ resistance for NH₃-SCR at low temperature, *Chem. Eng. J.*, 2019, **370**, 897–905.

14 U. Hennings and R. Reimert, Investigation of the structure and the redox behavior of gadolinium doped ceria to select a suitable composition for use as catalyst support in the steam reforming of natural gas, *Appl. Catal., A*, 2007, **325**, 41–49.

15 B. Jiang, B. Deng, Z. Zhang, Z. Wu, X. Tang, S. Yao and H. Lu, Effect of Zr Addition on the Low-Temperature SCR Activity and SO₂ Tolerance of Fe–Mn/Ti Catalysts, *J. Phys. Chem. C*, 2014, **118**, 14866–14875.

16 P. Maitarad, J. Han, D. Zhang, L. Shi, S. Namuangruk and T. Rungrotmongkol, Structure–Activity Relationships of NiO on CeO₂ Nanorods for the Selective Catalytic Reduction of NO with NH₃: Experimental and DFT Studies, *J. Phys. Chem. C*, 2014, **118**, 9612–9620.

17 L. Xiangwen, Z. Kebin, W. Lei, W. Baoyi and L. Yadong, Oxygen vacancy clusters promoting reducibility and activity of ceria nanorods, *J. Am. Chem. Soc.*, 2009, **131**, 3140–3141.

18 Z. Yan, Y. Qu, L. Liu, X. Ge, J. Yang, L. Wei, T. Yang and X. Wang, Promotional effect of rare earth-doped manganese oxides supported on activated semi-coke for selective catalytic reduction of NO with NH₃, *Environ. Sci. Pollut. Res. Int.*, 2017, **24**, 24473–24484.

19 C. Yu, B. Huang, L. Dong, F. Chen, Y. Yang, Y. Fan, Y. Yang, X. Liu and X. Wang, Effect of Pr/Ce addition on the catalytic performance and SO₂ resistance of highly dispersed MnOₓ/SAPO-34 catalyst for NH₃-SCR at low temperature, *Chem. Eng. J.*, 2017, **316**, 1059–1068.

20 R.-t. Guo, Q.-l. Chen, H.-l. Ding, Q.-s. Wang, W.-g. Pan, N.-z. Yang and C.-z. Lu, Preparation and characterization of CeOₓ@MnOₓ core–shell structure catalyst for catalytic oxidation of NO, *Catal. Commun.*, 2015, **69**, 165–169.

21 X. W. Lou, L. A. Archer and Z. Yang, Hollow Micro-/Nanostructures: Synthesis and Applications, *Adv. Mater.*, 2008, **20**, 3987–4019.

22 J. Yu, F. Guo, Y. Wang, J. Zhu, Y. Liu, F. Su, S. Gao and G. Xu, Sulfur poisoning resistant mesoporous Mn-base catalyst for low-temperature SCR of NO with NH₃, *Appl. Catal., B*, 2010, **95**, 160–168.

23 S. Zhan, M. Qiu, S. Yang, D. Zhu, H. Yu and Y. Li, Facile preparation of MnO₂ doped Fe₂O₃ hollow nanofibers for low temperature SCR of NO with NH₃, *J. Mater. Chem. A*, 2014, **2**, 20486–20493.

24 L. Zhang, L. Shi, L. Huang, J. Zhang, R. Gao and D. Zhang, Rational Design of High-Performance DeNOx Catalysts Based on MnxCo₃₋ₓO₄ Nanocages Derived from Metal–Organic Frameworks, *ACS Catal.*, 2014, **4**, 1753–1763.

25 L. Han, M. Gao, J. Y. Hasegawa, S. Li, Y. Shen, H. Li, L. Shi and D. Zhang, SO₂-Tolerant Selective Catalytic Reduction of NOₓ over Meso-TiO₂@Fe₂O₃@Al₂O₃ Metal-Based Monolith Catalysts, *Environ. Sci. Technol.*, 2019, **53**, 6462–6473.

26 K. Ma, W. Zou, L. Zhang, L. Li, S. Yu, C. Tang, F. Gao and L. Dong, Construction of hybrid multi-shell hollow structured CeO₂–MnOₓ materials for selective catalytic reduction of NO with NH₃, *RSC Adv.*, 2017, **7**, 5989–5999.

27 X. Sun and Y. Li, Colloidal carbon spheres and their core/shell structures with noble-metal nanoparticles, *Angew. Chem., Int. Ed. Engl.*, 2004, **43**, 597–601.

28 W. Li, C. Zhang, X. Li, P. Tan, A. Zhou, Q. Fang and G. Chen, Ho-modified Mn-Ce/TiO₂ for low-temperature SCR of NO with NH₃: evaluation and characterization, *Chin. J. Catal.*, 2018, **39**, 1653–1663.

29 X. Yao, J. Cao, L. Chen, K. Kang, Y. Chen, M. Tian and F. Yang, Doping effect of cations (Zr⁴⁺, Al³⁺, and Si⁴⁺) on MnO/CeO₂ nano-rod catalyst for NH₃-SCR reaction at low temperature, *Chin. J. Catal.*, 2019, **40**, 733–743.

30 X. Yao, L. Chen, J. Cao, Y. Chen, M. Tian, F. Yang, J. Sun, C. Tang and L. Dong, Enhancing the deNO performance of MnO/CeO₂-ZrO₂ nanorod catalyst for low-temperature NH₃-SCR by TiO₂ modification, *Chem. Eng. J.*, 2019, **369**, 46–56.

31 S. Liang, F. Teng, G. Bulgan, R. Zong and Y. Zhu, Effect of Phase Structure of MnO₂ Nanorod Catalyst on the Activity for CO Oxidation, *J. Phys. Chem. C*, 2010, **112**, 5307–5315.

32 J. Xu, Y. Sun, M. Lu, L. Wang, J. Zhang, J. Qian and E. J. Kim, Fabrication of porous Mn₂O₃ microsheet arrays on nickel foam as high-rate electrodes for supercapacitors, *J. Alloys Compd.*, 2017, **717**, 108–115.

33 M. F. Gazulla, M. J. Ventura, C. Andreu, J. Gilabert, M. Orduña and M. Rodrigo, Praseodymium oxides. Complete characterization by determining oxygen content, *Microchem. J.*, 2019, **148**, 291–298.

34 P. Monica and M. Kakihana, Praseodymium oxide formation by thermal decomposition of a praseodymium complex, *Solid State Ionics*, 2001, **141–142**, 265–272.

35 B. Mutharani, P. Ranganathan, S. M. Chen and P. Sireesha, Ultrasound-induced radicals initiated the formation of inorganic-organic Pr₂O₃/polystyrene hybrid composite for electro-oxidative determination of chemotherapeutic drug methotrexate, *Ultrason. Sonochem.*, 2019, **56**, 410–421.

36 H. Wang, Z. Zhang, C. Dong, G. Chen, Y. Wang and H. Guan, Carbon spheres@MnO₂ core-shell nanocomposites with enhanced dielectric properties for electromagnetic shielding, *Sci. Rep.*, 2017, **7**, 15841.

37 K. Lei, L. Cong, X. Fu, F. Cheng and J. Chen, Stirring-assisted hydrothermal synthesis of ultralong α-MnO₂ nanowires for oxygen reduction reaction, *Inorg. Chem. Front.*, 2016, **3**, 928–933.

38 Y.-C. Zhang, J.-T. Li, Z.-G. Wu, L. Huang and S.-G. Sun, Synthesis of hierarchical spindle-like Mn₂O₃ for lithium ion batteries with enhanced lithium storage properties, *J. Alloys Compd.*, 2017, **721**, 229–235.

39 T. Du, H. Qu, Q. Liu, Q. Zhong and W. Ma, Synthesis, activity and hydrophobicity of Fe-ZSM-5@silicalite-1 for NH₃-SCR, *Chem. Eng. J.*, 2015, **262**, 1199–1207.

40 B. Shen, F. Wang and T. Liu, Homogeneous MnO–CeO₂ pellets prepared by a one-step hydrolysis process for low-temperature NH₃-SCR, *Powder Technol.*, 2014, **253**, 152–157.

41 J. Wang, Z. Yan, L. Liu, Y. Zhang, Z. Zhang and X. Wang, Low-temperature SCR of NO with NH_3 over activated semi-coke composite-supported rare earth oxides, *Appl. Surf. Sci.*, 2014, **309**, 1–10.

42 F. Gao, X. Tang, H. Yi, J. Li, S. Zhao, J. Wang, C. Chu and C. Li, Promotional mechanisms of activity and SO_2 tolerance of Co- or Ni-doped MnO_x-CeO_2 catalysts for SCR of NO_x with NH_3 at low temperature, *Chem. Eng. J.*, 2017, **317**, 20–31.

43 Z. Liu, Y. Yi, S. Zhang, T. Zhu, J. Zhu and J. Wang, Selective catalytic reduction of NO_x with NH_3 over Mn-Ce mixed oxide catalyst at low temperatures, *Catal. Today*, 2013, **216**, 76–81.

44 Y. Su, B. Fan, L. Wang, Y. Liu, B. Huang, M. Fu, L. Chen and D. Ye, MnO_x supported on carbon nanotubes by different methods for the SCR of NO with NH_3, *Catal. Today*, 2013, **201**, 115–121.

45 L. Wang, B. Huang, Y. Su, G. Zhou, K. Wang, H. Luo and D. Ye, Manganese oxides supported on multi-walled carbon nanotubes for selective catalytic reduction of NO with NH_3: catalytic activity and characterization, *Chem. Eng. J.*, 2012, **192**, 232–241.

46 H. Chang, T. Zhang, H. Dang, X. Chen, Y. You, J. W. Schwank and J. Li, Fe_2O_3@SiTi core–shell catalyst for the selective catalytic reduction of NO_x with NH_3: activity improvement and HCl tolerance, *Catal. Sci. Technol.*, 2018, **8**, 3313–3320.

47 Y. Chao, L. X. H. BiChun and W. YouMing, Structural Properties and Low-Temperature SCR Activity of Zirconium-Modified MnOx/MWCNTs Catalysts, *Acta Phys.-Chim. Sin.*, 2014, **30**, 1895–1920.

48 X. Du, C. Li, L. Zhao, J. Zhang, L. Gao, J. Sheng, Y. Yi, J. Chen and G. Zeng, Promotional removal of HCHO from simulated flue gas over Mn-Fe oxides modified activated coke, *Appl. Catal., B*, 2018, **232**, 37–48.

49 B. Zhao, H. Yi, X. Tang, Q. Li, D. Liu and F. Gao, Using CuO-MnO_x/AC-H as catalyst for simultaneous removal of Hg degrees and NO from coal-fired flue gas, *J. Hazard. Mater.*, 2019, **364**, 700–709.

50 F. Liu, H. He, Y. Ding and C. Zhang, Effect of manganese substitution on the structure and activity of iron titanate catalyst for the selective catalytic reduction of NO with NH_3, *Appl. Catal., B*, 2009, **93**, 194–204.

51 H. He, H. X. Dai, K. W. Wong and C. T. Au, $RE_{0.6}Zr_{0.4-x}Y_xO_2$ (RE = Ce, Pr; x = 0, 0.05) solid solutions: an investigation on defective structure, oxygen mobility, oxygen storage capacity, and redox properties, *Appl. Catal., A*, 2003, **251**, 61–74.

52 C. K. Narula, L. P. Haack, W. Chun, H.-W. Jen and G. W. Graham, Single-Phase PrOy-ZrO_2 Materials and Their Oxygen Storage Capacity: A Comparison with Single-Phase CeO_2-ZrO_2, PrOy-CeO_2, and PrOy-CeO_2-ZrO_2 Materials, *J. Phys. Chem. B*, 1999, **103**, 3634–3639.

53 E. Poggio-Fraccari, G. Baronetti and F. Mariño, Pr^{3+} surface fraction in CePr mixed oxides determined by XPS analysis, *J. Electron Spectrosc. Relat. Phenom.*, 2018, **222**, 1–4.

54 Z. Song, W. Liu, H. Nishiguchi, A. Takami, K. Nagaoka and Y. Takita, The Pr promotion effect on oxygen storage capacity of Ce–Pr oxides studied using a TAP reactor, *Appl. Catal., A*, 2007, **329**, 86–92.

55 X. Lu, C. Song, S. Jia, Z. Tong, X. Tang and Y. Teng, Low-temperature selective catalytic reduction of NO_x with NH_3 over cerium and manganese oxides supported on TiO_2–graphene, *Chem. Eng. J.*, 2015, **260**, 776–784.

56 L. Zhang, D. Zhang, J. Zhang, S. Cai, C. Fang, L. Huang, H. Li, R. Gao and L. Shi, Design of meso-TiO_2@MnO(x)-CeO(x)/CNTs with a core-shell structure as DeNO(x) catalysts: promotion of activity, stability and SO_2-tolerance, *Nanoscale*, 2013, **5**, 9821–9829.

57 Z. Fan, J.-W. Shi, C. Gao, G. Gao, B. Wang, Y. Wang, C. He and C. Niu, Gd-modified MnO_x for the selective catalytic reduction of NO by NH_3: the promoting effect of Gd on the catalytic performance and sulfur resistance, *Chem. Eng. J.*, 2018, **348**, 820–830.

58 Z. Ma, X. Wu, Y. Feng, Z. Si and D. Weng, Effects of WO_3 doping on stability and N_2O escape of MnO_x–CeO_2 mixed oxides as a low-temperature SCR catalyst, *Catal. Commun.*, 2015, **69**, 188–192.

59 M. Richter, A. Trunschke, U. Bentrup, K. W. Brzezinka, E. Schreier, M. Schneider, M. M. Pohl and R. Fricke, Selective Catalytic Reduction of Nitric Oxide by Ammonia over Egg-Shell MnO_x/NaY Composite Catalysts, *J. Catal.*, 2002, **206**, 98–113.

60 P. M. Sreekanth and P. G. Smirniotis, Selective Reduction of NO with CO Over Titania Supported Transition Metal Oxide Catalysts, *Catal. Lett.*, 2007, **122**, 37–42.

61 X. Tang, Y. Li, X. Huang, Y. Xu, H. Zhu, J. Wang and W. Shen, MnO_x–CeO_2 mixed oxide catalysts for complete oxidation of formaldehyde: effect of preparation method and calcination temperature, *Appl. Catal., B*, 2006, **62**, 265–273.

62 B. Thirupathi and P. G. Smirniotis, Effect of Nickel as Dopant in Mn/TiO_2 Catalysts for the Low-Temperature Selective Reduction of NO with NH_3, *Catal. Lett.*, 2011, **141**, 1399–1404.

63 J. Trawczyński, B. Bielak and W. Miśta, Oxidation of ethanol over supported manganese catalysts—effect of the carrier, *Appl. Catal., B*, 2005, **55**, 277–285.

64 V. Frizon, J.-M. Bassat, M. Pollet, E. Durand, J. Hernandez, K. Pajot, P. Vernoux and A. Demourgues, Tuning the Pr Valence State To Design High Oxygen Mobility, Redox and Transport Properties in the CeO_2–ZrO_2–PrO_x Phase Diagram, *J. Phys. Chem. C*, 2019, **123**, 6351–6362.